

# On the Feasibility of Pairing Pyrochlore Iron(III) Hydroxy Fluoride Cathode with Argyrodite $\text{Li}_6\text{PS}_5\text{Cl}$ Solid-State Electrolyte for Low-Cost All-Solid-State Batteries

Jaka Sivavec,<sup>[a, b]</sup> Julian F. Baumgärtner,<sup>[a, b]</sup> Dragos C. Stoian,<sup>[c]</sup> Matthias Klimpel,<sup>[a, b]</sup> Wouter van Beek,<sup>[c]</sup> Maksym V. Kovalenko,<sup>\*[a, b]</sup> and Kostiantyn V. Kravchyk<sup>[a, b]</sup>

As demand for low-cost, high-energy-density all-solid-state batteries continues to rise, exploring novel cathodes composed of earth-abundant elements is imperative. Iron hydroxy fluorides with the pyrochlore structure (Pyr-IHF) emerge as compelling cathode materials due to abundant natural reserves of their constituent elements, high energy density, and rate capability. In this work, we explore the viability of Pyr-IHF as a cathode material in all-solid-state batteries when paired with argyrodite-type  $\text{Li}_6\text{PS}_5\text{Cl}$  (LPSCl) solid-state electrolyte. Our findings show that the Pyr-IHF/LPSCl cathode delivers a high

initial charge capacity of  $172 \text{ mAh g}^{-1}$  at a 0.1 C rate, with *ca.* 65% capacity retention after 50 cycles. Advanced characterization techniques, including focused ion beam-scanning electron microscopy, scanning electron microscopy coupled with energy dispersive X-ray spectroscopy, and X-ray absorption spectroscopy, indicate a pronounced redox reaction between Pyr-IHF and LPSCl upon cell preparation, resulting in significant capacity contributions from the sulfur redox of LPSCl decomposition products during electrochemical cycling.

## Introduction

Solid-state batteries based on argyrodite-type  $\text{Li}_6\text{PS}_5\text{Cl}$  (LPSCl) solid-state electrolytes (SSEs) have emerged as compelling electrochemical systems, gaining significant attention in recent years.<sup>[1]</sup> LPSCl SSEs offer several advantages, including high ionic conductivity, low electronic conductivity, low density, and low production costs. Unlike oxide SSEs that require high temperatures for sintering,<sup>[2]</sup> argyrodite SSEs exhibit high ductility. This allows for the fabrication of argyrodite-based cathodes using a facile cold isostatic pressing technique, which is key for achieving intimate contact with the cathode active materials at room temperature.<sup>[1b]</sup>

Among the various cathode materials that have been explored in combination with argyrodite SSEs,  $\text{LiNi}_x\text{Mn}_y\text{Co}_{1-x-y}\text{O}_2$  (NMC),<sup>[3]</sup> has shown some of the highest electrochemical performance. NMC-based full cells have demonstrated stable operation for up to 1000 cycles, delivering a capacity of  $>200 \text{ mAh g}^{-1}$  at high cathode loadings ( $6.8 \text{ mAh cm}^{-2}$ ).<sup>[3b]</sup> However, the demand for Co and Ni contained within NMC could surpass production capacity within the next two decades, potentially leading to cobalt shortages by 2030<sup>[4]</sup> and nickel shortages by 2037.<sup>[5]</sup> In light of these projections, there is increasing interest in developing cathode materials from earth-abundant elements to reduce costs and ensure the sustainability of all-solid-state batteries, including  $\text{LiMn}_2\text{O}_4$ ,<sup>[3a]</sup> and  $\text{LiFePO}_4$ ,<sup>[6]</sup> and iron(III) fluorides (IF).<sup>[7]</sup> Among these, IF derivatives are particularly attractive due to their non-toxicity and their high oxidative stability,<sup>[8]</sup> while offering a high theoretical capacity of around  $237 \text{ mAh g}^{-1}$  for the one-electron redox process.<sup>[9]</sup>

The electrochemical performance of IF in combination with argyrodite SSEs was first reported by Wu *et al.* in 2023,<sup>[7a]</sup> showcasing stable charge storage capacities of around  $400 \text{ mAh g}^{-1}$  for a three-electron process over 300 cycles. Despite these compelling results, the underlying mechanisms responsible for the charge storage capacity in solid-state IF/argyrodite SSE cathodes have not yet been thoroughly investigated, particularly in light of the potential capacity contributions from sulfur redox.<sup>[10]</sup>

Encouraged by initial reports on the electrochemical performance of argyrodite-based IF cathodes, we sought to investigate their redox chemistry further. Given the high  $\text{Li}^+$  ion diffusion in IF/iron hydroxy fluorides(IHF) with a pyrochlore-type structure, due to the presence of large hexagonal channels formed by corner-shared  $\text{FeF}_6/\text{Fe}(\text{F}/\text{OH})_6$  octahedra, which are

[a] J. Sivavec, J. F. Baumgärtner, M. Klimpel, M. V. Kovalenko, K. V. Kravchyk  
Laboratory for Thin Films and Photovoltaics, Empa – Swiss Federal Laboratories for Materials Science and Technology, Überlandstrasse 129, CH-8600 Dübendorf, Switzerland  
E-mail: mvkovalenko@ethz.ch  
Kostiantyn.Kravchyk@empa.ch

[b] J. Sivavec, J. F. Baumgärtner, M. Klimpel, M. V. Kovalenko, K. V. Kravchyk  
Laboratory of Inorganic Chemistry, Department of Chemistry and Applied Biosciences, ETH Zürich, Vladimir-Prelog-Weg 1, CH-8093 Zürich, Switzerland

[c] D. C. Stoian, W. van Beek  
Swiss-Norwegian Beamlines, European Synchrotron Radiation Facility, Grenoble 38000, France

 Supporting information for this article is available on the WWW under <https://doi.org/10.1002/batt.202400731>

 © 2024 The Author(s). *Batteries & Supercaps* published by Wiley-VCH GmbH. This is an open access article under the terms of the Creative Commons Attribution Non-Commercial License, which permits use, distribution and reproduction in any medium, provided the original work is properly cited and is not used for commercial purposes.

hypothesised to act as  $\text{Li}^+$  diffusion pathways,<sup>[11]</sup> we focused on studying pyrochlore IHF in this work. Additionally, as demonstrated in our recent study, pyrochlore-type iron hydroxy fluoride (Pyr-IHF) can be synthesized in the form of monodisperse spherical particles with an average size of 250 nm, exhibiting minimal volume expansion upon lithiation, making them well-suited for use in solid-state cathodes.<sup>[12]</sup> The redox mechanism of the prepared cathodes was analyzed using scanning electron microscopy (SEM), energy-dispersive X-ray (EDX) spectroscopy, and X-ray absorption spectroscopy (XAS). Our findings suggest a pronounced chemical reaction between Pyr-IHF and LPSCI (Figure 1a), causing significant structural changes on an atomic and particle level, and resulting in significant capacity contribution from sulfur redox.

## Results and Discussion

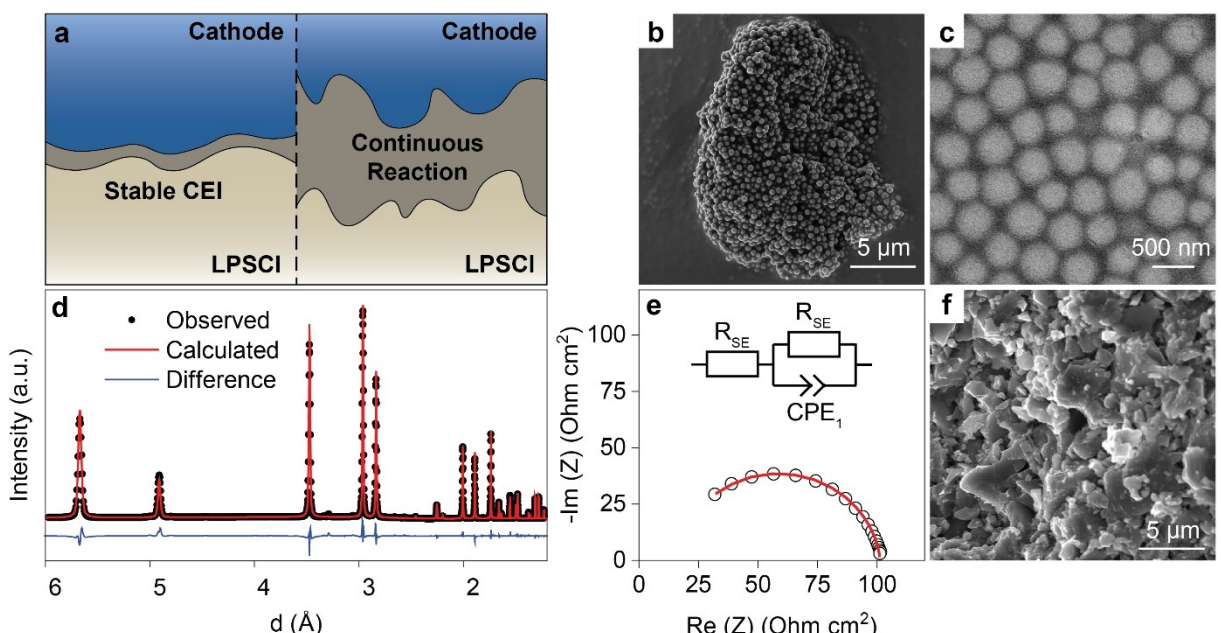
Pyr-IHF with a nominal composition of  $\text{FeF}_2(\text{OH}) \cdot 0.4 \text{ H}_2\text{O}$  was synthesized following our previously reported method.<sup>[11a]</sup> In short, the  $\text{FeF}_3(\text{H}_2\text{O})_2 \cdot \text{H}_2\text{O}$  precursor was partially dissolved in ethanol, and a small quantity of water was then added to induce precipitation of the Pyr-IHF. Upon water addition, individual  $\text{Fe}(\text{F}/\text{OH})_6$  octahedra condensed with water acting as a templating agent, resulting in the crystallization of the cubic pyrochlore structure ( $\text{Fd}-3\text{m}$ ).<sup>[13]</sup> Subsequently, the precipitated Pyr-IHF powder was dried under vacuum and heat-treated at 280°C for 1 hour under a nitrogen atmosphere in order to remove the accessible structural water. This results in the formation of a final product with the nominal composition of  $\text{FeF}_2(\text{OH}) \cdot 0.2 \text{ H}_2\text{O}$ . As follows from X-ray powder diffraction (XRPD) patterns and scanning electron microscopy (SEM) micro-

graphs shown in Figure S1 and Figures 1b, c, respectively, the as-synthesized Pyr-IHF powder consisted of polycrystalline spherical nanoparticles of ca. 250 nm with a narrow particle size distribution.

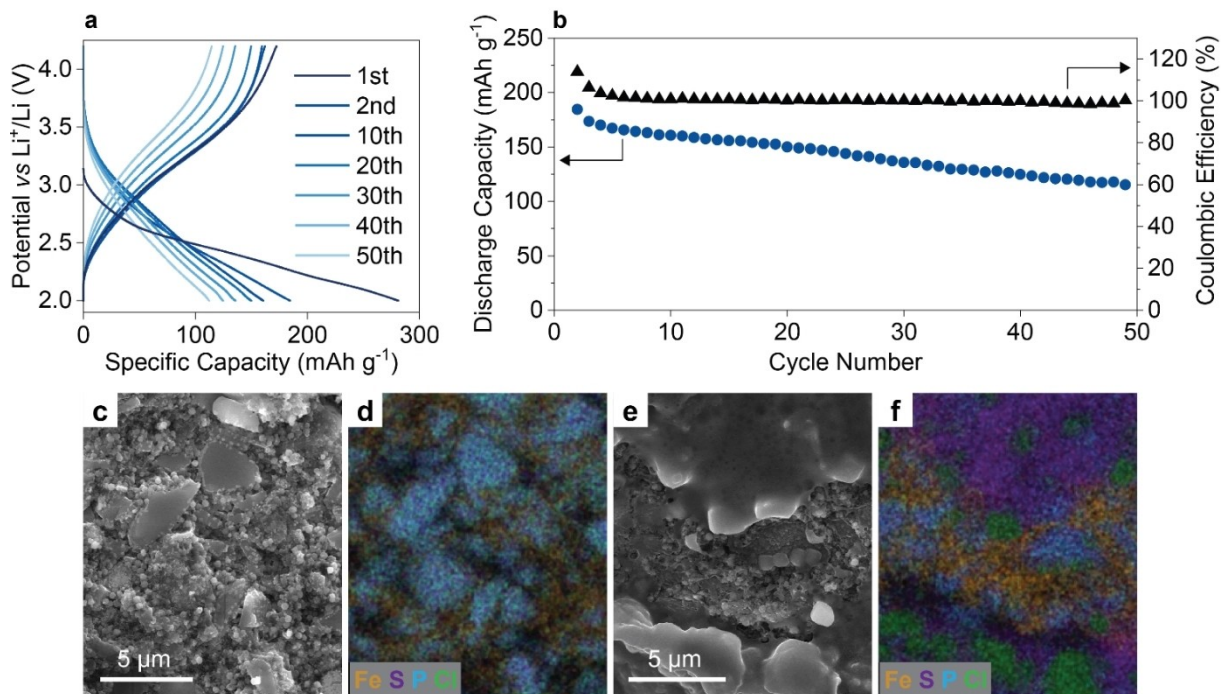
The electrochemical performance of Pyr-IHF was investigated in combination with LPSCI SSE, which was characterised prior to cell assembly to confirm its phase purity, particle size distribution and high ionic conductivity (Figure 1d, e, f). Pyr-IHF was ball-milled with LPSCI solid-state electrolyte and carbon black as a conductive additive. The full cells were then assembled by uniaxial pressing of the Pyr-IHF solid-state cathode powder with LPSCI solid-state electrolyte powder and Li–In foil discs as the negative electrode, and cycled in cylindrical cells under a pressure of 6 MPa.

Figure 2a shows the voltage profiles of the Pyr-IHF-containing cathodes cycled between 2.0 and 4.2 V at 0.1 C rate ( $\approx 18 \text{ mA g}^{-1}$ ). The initial discharge and charge capacities were  $281 \text{ mAh g}^{-1}$  and  $172 \text{ mAh g}^{-1}$ , respectively, corresponding to an initial coulombic efficiency of 163%. Subsequently, the coulombic efficiency improved significantly and approached ca. 99% for the following 50 cycles. The specific charge storage capacity during the first charge was equal to 74% of the theoretical capacity ( $234 \text{ mAh g}^{-1}$ ) and was comparable to the experimentally determined capacity previously reported in liquid electrolyte cells (Figure 2b).<sup>[11a]</sup>

To comprehend the morphological and chemical changes occurring during cycling of Pyr-IHF cathodes, SEM-EDX analysis was performed on both pristine and cycled cathodes after five cycles. As evident from the high-resolution SEM micrographs (Figure 2c and Figure S2a) and EDX analysis (Figure 2d) of the pristine Pyr-IHF solid-state cathode, the morphology of Pyr-IHF particles remained largely intact after cathode preparation,



**Figure 1.** Material Characterisation. a) Schematic representation of a stable (left) and unstable (right) cathode electrolyte combination. b,c) SEM micrographs of the as-prepared Pyr-IHF active material. d) SXRD pattern of the as-purchased LPSCI. e) EIS measurement of a  $\text{Li}|\text{LPSCI}|\text{Li}$  symmetrical cell. f) SEM micrograph of a cut LPSCI separator pellet after densification at 390 MPa.



**Figure 2.** Electrochemical Performance and SEM-EDX Mapping of Pyr-IHF/LPSCI solid-state cathode. a-b) Evolution of the voltage profiles (a) and cycling stability (b) of a Li-In|LPSCI|Pyr-IHF full cell cycled at 0.1 C rate ( $18 \text{ mA g}^{-1}$ ). c-d) SEM micrograph (c) and the corresponding EDX map (d) of the pristine cathode. e-f) SEM micrograph (e) and the corresponding EDX map (f) of the cathode after 5 cycles.

consistent with the as-synthesized Pyr-IHF. The individual LPSCI and Pyr-IHF particles are clearly distinguishable based on their morphology, with a distinct spatial separation of Fe from P, S, and Cl. The complete overlap of P, S, and Cl elements also indicates that the LPSCI solid-state electrolyte remains mostly intact following cathode preparation.

In stark contrast to the pristine state, electrochemical cycling induces significant degradation of the Pyr-IHF cathode components (Figures 2e, f) with neither the Pyr-IHF, nor the LPSCI retaining their particle morphology. Furthermore, the nearly complete spatial separation of S, P, and Cl (Figure S5) within the cathode likely indicates the formation of S, LiCl, and  $\text{P}_2\text{S}_5$  rich domains via an oxidative decomposition of LPSCI.<sup>[14]</sup> Surprisingly, the initially well-distributed Pyr-IHF particles also agglomerate, as evidenced by the concentrated Fe domains in the cycled cathode. Contrary to this, the Pyr-IHF particles maintain their spatial separation and particle morphology when cycled in liquid electrolytes.<sup>[12]</sup> Moreover, the LPSCI and Pyr-IHF particles fuse together during cycling, as shown by post-mortem FIB-SEM (Figure S2b). Overall, these results suggest that Pyr-IHF critically affects LPSCI degradation during cycling.

As the sulfur in LPSCI decomposition products can be redox active, it may give rise to additional charge storage capacity. To discriminate between the capacity contributions from S and Fe-based redox processes, the Fe K-edge X-ray Absorption Near Edge Spectroscopy (XANES) spectra of Pyr-IHF cathodes were acquired at different states of charge, and compared to reference spectra of Pyr-IHF cathodes cycles in an ionic liquid electrolyte (Figures 3a-f). In the liquid electrolyte a significant edge shift of 5 eV during lithiation is observed, demonstrating

the sole capacity contribution from the reduction of Fe(III) to Fe(II). In the subsequent charge, the spectrum of the as-prepared cathode is nearly completely recovered, indicating the high reversibility of the redox process. In contrast, a noteworthy decrease of 2 eV in the Fe K-edge position is observed between the as-synthesized Pyr-IHF and the pristine solid-state cathode. The shifts during the first discharge and charge are significantly smaller, specifically less than 0.1 eV, and 0.5 eV, respectively. The 0.5 eV increase during the charge indicates Fe redox activity, however as the shift observed during the preceding discharge is negligible, the Fe centres had to be partially reduced during cathode preparation. Yet the XAS spectrum of the pristine Pyr-IHF is not fully recovered after the first charge, which indicates that a change in the chemical environment of Fe has also occurred. This suggests that a redox reaction occurs between Pyr-IHF and LPSCI during cathode preparation. The minor redox changes associated with Fe during cycling are in contrast with the high electrochemical capacity that is observed, and further suggest that S redox significantly contributes to the observed capacity.

Intrigued by these results, we further investigated the atomic level structural changes that Fe undergoes during cycling using Extended X-ray Absorption Fine Structure (EXAFS) analysis. In the liquid electrolyte cells the first shell Fe–L (where L refers to a ligand) bond distance increases by 0.1 Å during the first discharge and contracts by 0.07–0.08 Å during the subsequent charge, reflecting the highly reversible changes in the Fe oxidation state. Conversely, a 0.2 Å expansion occurs during the preparation of the solid-state cathode. This considerable elongation of the Fe–L bonds is not consistent with the

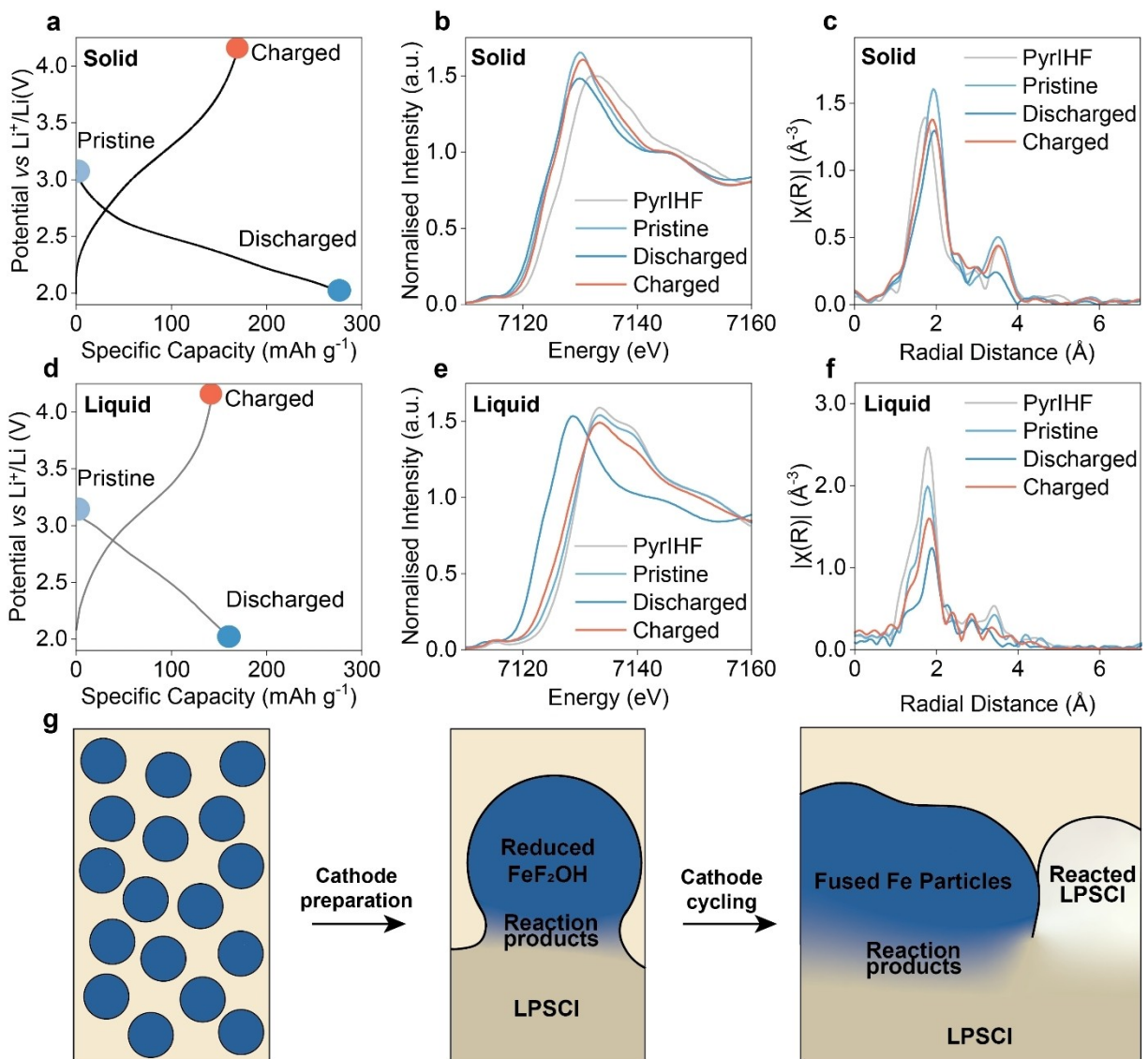


**Figure 3.** X-Ray Absorption Spectroscopy Measurements of Conventional Pyr-IHF and Pyr-IHF/LPSCI Solid-State Cathodes at Different States of Charge. a–c) A characteristic voltage profile of a Pyr-IHF cathode in a LiTFSI liquid electrolyte cell (a) with the corresponding XANES (b) and EXAFS (c) spectra at different states of charge. d–f) A characteristic voltage profile of a Pyr-IHF/LPSCI solid-state cathode (d) with the corresponding XANES (e) and EXAFS (f) spectra at different states of charge. (g) Schematic representation of the extent of the side reactions in a Pyr-IHF and LPSCI composite cathode during cathode preparation and electrochemical cycling.

reduction of  $\text{Fe(III)(F/OH)}_6$  to  $\text{Fe(II)(F/OH)}_6$  which is observed in the liquid system. Therefore, in light of the chemical reaction between Pyr-IHF and LPSCI, ligand exchange accompanied by partial Fe reduction provides a reasonable explanation for the bond distance changes.

These results suggest that during cathode preparation, oxidative decomposition of LPSCI in the presence of Pyr-IHF leads to the reduction of the Fe centers and the formation of oxidized sulfur species, which are reduced to  $\text{S}^{2-}$  during the first discharge. In the subsequent charge, both Fe and S species are likely redox active and contribute to the observed capacity. A schematic representation of this process is shown in Figure 3g. The role of the Pyr-IHF in enabling the reversible capacity is further supported by a reference experiment in which a cathode mixture containing only LPSCI and carbon was

prepared and cycled under the same conditions (Figure S6). In this case only minor capacities were recorded during the first charge and discharge. These observations are consistent with recent finding by Shao *et al.*,<sup>[15]</sup> who investigated the conversion process of  $\text{FeF}_2$  cathodes in combination with  $\text{Li}_2\text{S}-\text{P}_2\text{S}_5$  (LPS)<sup>-</sup>LISICON-type sulfide-based electrolytes. Their XAS and X-ray photoelectron spectroscopy spectra demonstrated that  $\text{FeF}_2$  and LPS react upon contact, forming  $\text{FeS}$ , reduced P, and oxidized S species. This reaction is further driven during electrochemical cycling, leading to the depletion of  $\text{FeF}_2$  active material.

## Conclusions

In summary, we assess the electrochemical compatibility of Pyr-IHF as a cathode active material with the argyrodite LPSCI solid-state catholyte. Our findings show that Pyr-IHF/LPSCI cathodes exhibit high initial discharge and charge capacities of  $281 \text{ mAh g}^{-1}$  and  $172 \text{ mAh g}^{-1}$ , respectively, at a 0.1 C rate, with 65% capacity retention over 50 cycles. The combined SEM, EDX, and XAS analysis indicates that a redox reaction between Pyr-IHF and LPSCI occurs during cathode preparation, leading to the reduction of Pyr-IHF, changes in Fe coordination, and the formation of oxidized sulfur species. These findings suggest that both Fe and S species are redox-active, contributing to the charge capacity of the Pyr-IHF/LPSCI cathode. This work highlights the reactivity between iron fluoride-based cathode materials and the LPSCI SSE. In the absence of protective interfacial layers, the employment of iron fluoride cathodes in combination with LPSCI solid-state electrolytes might be challenging. Furthermore, similar issues could arise with other Fe-based cathodes (for instance LiFePO<sub>4</sub>), which should be considered in the future design of solid-state battery systems.

## Experimental Section

### Synthesis of Pyr-IHF

The Pyr-IHF cathode material was synthesised as reported previously.<sup>[11a]</sup> In short,  $\text{FeF}_3(\text{H}_2\text{O})_2 \cdot \text{H}_2\text{O}$  (0.5000 g, abcr chemicals) was added to EtOH (150 mL, 99.8%, EMSURE, ACS) in a 250 mL capped bottle. The suspension was stirred for 6 hours at room temperature. The solution was centrifuged (10000 rpm, 5 min) and filtered (PTFE syringe filter, 0.45  $\mu\text{m}$ ) to separate it from undissolved impurities. Afterwards, 6 mL of water was added to induce the precipitation of product. After 16–24 h, the suspension was again centrifuged (10000 rpm, 5 min) and the beige Pyr-IHF powder was collected and dried under vacuum ( $80^\circ\text{C}$ , 8 hours) followed by an additional heat treatment step at  $280^\circ\text{C}$  in inert atmosphere ( $\text{N}_2$  flow, 30 min,  $10^\circ\text{C min}^{-1}$  ramp).

### Preparation and Assembly of Electrochemical Cells

All cell preparation steps were carried out under inert conditions in an Ar-filled glovebox. Symmetrical  $\text{Li}|\text{LPSCI}|\text{Li}$  cells used for potentiostatic impedance spectroscopy were prepared by pressing 100 mg of LPSCI (KRI) inside an 8 mm pressing die at 2 t (390 MPa) for 3 min. The LPSCI pellet was then removed from the pressing die and transferred to a Sphere cell frame. 8 mm Li discs were attached to each side of the pellet at 75 MPa for 3 min.

The full cells based on liquid electrolyte were prepared and assembled as reported previously.<sup>[11a]</sup> Ionic liquid electrolytes were used due to their enhanced stability towards Pyr-IHF active material. The solid-state cathode composite was prepared by mixing Pyr-IHF, LPSCI, and carbon black Timcal C65 (40:52.5:7.5 mass ratio, 100 mg total mass) powders in a ball-mill (Fritsch Pulverisette 23, 15 Hz) for 15 min using a  $\text{ZrO}_2$  jar with  $\text{ZrO}_2$  balls (3 mm diameter, 5 g).

The assembly of solid-state full cells was made as follows. 100 mg of LPSCI powder was pressed in a 8 mm pressing die by hand to create a flat surface. Afterwards, 1.5–1.7 mg of the cathode composite was added on one side (ca.  $1.3 \text{ mg cm}^{-2}$  Pyr-IHF loading)

of the formed LPSCI pellet and pressed at 2 t (390 MPa) for 3 min. Then, an 8 mm Li disc was sandwiched between two 8 mm In discs and attached to the other side of the pellet cell. To allow for Li–In alloy formation, the assembled cell was placed into a solid-state cell holder (Sphere, ASC–A+), and 50 MPa of pressure was applied for 2 hours. After this, the pressure was adjusted to 6 MPa for electrochemical cycling.

### Powder Synchrotron X-Ray Diffraction

Powder SXRD was performed at the BM01 beamline at the European Synchrotron Radiation Facility using the PILATUS@SNBL diffractometer ( $\lambda = 0.72020 \text{ \AA}$ ). Samples were prepared inside an Ar filled glovebox and flame-sealed inside 0.5 mm borosilicate capillaries. The Rietveld refinement was performed using GSAS-II software.<sup>[16]</sup> Instrumental parameters were determined with a  $\text{LaB}_6$  NIST standard.

### X-Ray Absorption Spectroscopy

X-ray absorption measurements of the Fe K-edge were performed at the BM31 beamline at the European Synchrotron Radiation Facility using monochromated X-ray light. The liquid cell samples were previously measured at the same beamline.<sup>[12]</sup> Due to the thickness of the solid-state cells, all Pyr-IHF solid-state cathode samples were measured in fluorescence mode. The pellet-like cells were removed from the cell housing after electrochemical cycling and vacuum sealed in plastic foil inside an Ar-filled glovebox to ensure an inert environment was maintained throughout the measurement. The as-synthesized Pyr-IHF reference sample was prepared similarly by mixing 10 mg of the as-synthesized Pyr-IHF with 90 mg of cellulose powder and pressing the mixture into 8 mm diameter pellets. Spectra were recorded in the range of 7.0–8.0 keV. Data analysis was performed using the Demeter software package and a self-absorption correction was applied to the data collected for the solid-state samples.<sup>[17]</sup>

### Electron Microscopy

SEM measurements were performed on a ZEISS Gemini SEM 460 (5 kV acceleration voltage, 100 pA beam current), equipped with a EDS Ultime Extreme detector for EDX measurements. An inert transfer chamber was used for sample loading to avoid exposure to air. Cross-section FIB-SEM images were recorded on a Thermo Fisher Scientific Helios 5 Hydra Multi-Ion-Species Plasma FIB Microscope. To increase the cross-section quality a 5  $\mu\text{m}$  thick layer was deposited on the surface. For this, the gas injection system with 2% flow rate of the carbon pre-cursor and 100% of the W precursor was used, in combination with the Xe ion beam at 12 kV acceleration voltage and 20 nA current. The cross-sections were prepared by Xe ion beam milling with an acceleration voltage of 30 kV and a current of up to 0.2  $\mu\text{A}$ . The SEM micrographs were recorded using the through-the-lens detector in secondary electron mode at an electron beam acceleration voltage of 5 kV and 100 pA current.

### Electrochemical Measurements

Potentiostatic impedance spectroscopy of  $\text{Li}|\text{LPSCI}|\text{Li}$  symmetrical cells was performed on a SAS MTZ-35 impedance analyser in the frequency range between 10 MHz – 1 Hz with a peak amplitude of 10 mV. Galvanostatic cycling of full cells was performed in the voltage range between 1.4 – 3.6 V vs  $\text{Li}|\text{In}/\text{Li}^+$  (2.0 – 4.2 V vs  $\text{Li}/\text{Li}^+$ )

on an Astrol BAT-Flex potentiostat. Measurements were performed at room temperature and a current density of  $18 \text{ mA g}^{-1}$ .

## Author Contributions

The manuscript was written through the contributions of all authors. All authors have given approval to the final version of the manuscript.

## Acknowledgements

This work was financially supported by the Swiss Innovation Agency (Innosuisse) under grant agreement 58207.1. The authors thank the Swiss Norwegian beamlines at the ESRF. The authors are grateful to the research facilities at ETH Zurich, specifically the Scientific Center for Optical and Electron Microscopy and the Small Molecule Crystallography Center. They also acknowledge the research resources at Empa, particularly the Electron Microscopy Center.

## Conflict of Interests

The authors declare no conflict of interest.

## Data Availability Statement

The data that support the findings of this study are available from the corresponding author upon reasonable request.

**Keywords:** Solid-State Batteries • Pyrochlore Iron(III) Hydroxy Fluoride • Cathode • Argyrodite Li<sub>6</sub>PS<sub>5</sub>Cl Solid-State Electrolyte

- [1] a) H. J. Deiseroth, S. T. Kong, H. Eckert, J. Vannahme, C. Reiner, T. Zaiß, M. Schlosser, *Angew. Chem. Int. Ed. Engl.* **2008**, *47*, 755–758; b) C. Wang, J. Liang, Y. Zhao, M. Zheng, X. Li, X. Sun, *Energy Environ. Sci.* **2021**, *14*, 2577–2619; c) M. A. Kraft, S. P. Culver, M. Calderon, F. Böcher, T. Krauskopf, A. Senyshyn, C. Dietrich, A. Zevalkink, J. Janek, W. G. Zeier, *J. Am. Chem. Soc.* **2017**, *139*, 10909–10918; d) S. Wenzel, S. J. Sedlmaier, C. Dietrich, W. G. Zeier, J. Janek, *Solid State Ionics* **2018**, *318*, 102–112; e) C. Yu, L. van Eijck, S. Ganapathy, M. Wagemaker, *Electrochim. Acta* **2016**, *215*, 93–99; f) C. Yu, S. Ganapathy, J. Hageman, L. van Eijck, E. R. H. van Eck, L. Zhang, T. Schwietert, S. Basak, E. M. Kelder, M. Wagemaker,

*ACS Appl. Mater. Interfaces* **2018**, *10*, 33296–33306; g) F. Zhao, J. Liang, C. Yu, Q. Sun, X. Li, K. Adair, C. Wang, Y. Zhao, S. Zhang, W. Li, S. Deng, R. Li, Y. Huang, H. Huang, L. Zhang, S. Zhao, S. Lu, X. Sun, *Adv. Energy Mater.* **2020**, *10*, 1903422.

- [2] K. V. Kravchyk, D. T. Karabay, M. V. Kovalenko, *Sci. Rep.* **2022**, *12*, 1177.
- [3] a) J. Auvergniot, A. Cassel, J. B. Ledueil, V. Viallet, V. Seznec, R. Dedryvère, *Chem. Mater.* **2017**, *29*, 3883–3890; b) Y. G. Lee, S. Fujiki, C. Jung, N. Suzuki, N. Yashiro, R. Omoda, D. S. Ko, T. Shiratsuchi, T. Sugimoto, S. Ryu, J. H. Ku, T. Watanabe, Y. Park, Y. Aihara, D. Im, I. T. Han, *Nat. Energy* **2020**, *5*, 299–308; c) F. Walther, F. Strauss, X. Wu, B. Mogwitz, J. Hertle, J. Sann, M. Rohnke, T. Brezesinski, J. Janek, *Chem. Mater.* **2021**, *33*, 2110–2125.
- [4] a) X. Fu, D. N. Beatty, G. G. Gaustad, G. Ceder, R. Roth, R. E. Kirchain, M. Bustamante, C. Babbitt, E. A. Olivetti, *Environ. Sci. Technol.* **2020**, *54*, 2985–2993; b) A. Zeng, W. Chen, K. D. Rasmussen, X. Zhu, M. Lundhaug, D. B. Müller, J. Tan, J. K. Keiding, L. Liu, T. Dai, A. Wang, G. Liu, *Nat. Commun.* **2022**, *13*, 1341.
- [5] H. S. Shyam, I. Shuaib, S. P. Pandey, *Macromol. Symp.* **2023**, *407*, 2200068.
- [6] A. Cronk, Y.-T. Chen, G. Deysher, S.-Y. Ham, H. Yang, P. Ridley, B. Sayahpour, L. H. B. Nguyen, J. A. S. Oh, J. Jang, D. H. S. Tan, Y. S. Meng, *ACS Energy Lett.* **2023**, *8*, 827–835.
- [7] a) J. Peng, X. Wang, H. Li, L. Chen, F. Wu, *Adv. Energy Mater.* **2023**, *13*, 2300706; b) B. E. Murdock, K. E. Toghill, N. Tapia-Ruiz, *Adv. Energy Mater.* **2021**, *11*, 2102028; c) K. Lemoine, A. Hémon-Ribaud, M. Leblanc, J. Lhoste, J.-M. Tarascon, V. Maisonneuve, *Chem. Rev.* **2022**, *122*, 14405–14439.
- [8] a) G. G. Amatucci, N. Pereira, *J. Fluorine Chem.* **2007**, *128*, 243–262; b) X. Hua, A. S. Eggeman, E. Castillo-Martínez, R. Robert, H. S. Geddes, Z. Lu, C. J. Pickard, W. Meng, K. M. Wiaderek, N. Pereira, G. G. Amatucci, P. A. Midgley, K. W. Chapman, U. Steiner, A. L. Goodwin, C. P. Grey, *Nat. Mater.* **2021**, *20*, 841–850.
- [9] F. Wu, V. Srot, S. Chen, S. Lorger, P. A. van Aken, J. Maier, Y. Yu, *Adv. Mater.* **2019**, *31*, 1905146.
- [10] D. H. S. Tan, E. A. Wu, H. Nguyen, Z. Chen, M. A. T. Marple, J.-M. Doux, X. Wang, H. Yang, A. Banerjee, Y. S. Meng, *ACS Energy Lett.* **2019**, *4*, 2418–2427.
- [11] a) J. F. Baumgärtner, M. Wörle, C. P. Guntlin, F. Krumeich, S. Siegrist, V. Vogt, D. C. Stoian, D. Chernyshov, W. van Beek, K. V. Kravchyk, M. V. Kovalenko, *Adv. Mater.* **2023**, *35*, 2304158; b) C. Li, C. Yin, L. Gu, R. E. Dinnebier, X. Mu, P. A. van Aken, J. Maier, *J. Am. Chem. Soc.* **2013**, *135*, 11425–11428.
- [12] J. F. Baumgärtner, D. C. Stoian, K. P. Marhall, M. Jafarpour, M. Klimpel, H. Zhang, F. Okur, W. van Beek, D. Chernyshov, M. Wörle, M. V. Kovalenko, K. V. Kravchyk, *In review 2024*.
- [13] R. De Pape, G. Ferey, *Mater. Res. Bull.* **1986**, *21*, 971–978.
- [14] D. H. S. Tan, E. A. Wu, H. Nguyen, Z. Chen, M. A. T. Marple, J. M. Doux, X. Wang, H. Yang, A. Banerjee, Y. S. Meng, *ACS Energy Lett.* **2019**, 2418–2427.
- [15] B. Shao, S. Tan, Y. Huang, L. Zhang, J. Shi, X.-Q. Yang, E. Hu, F. Han, *Adv. Funct. Mater.* **2022**, *32*, 2206845.
- [16] B. H. Toby, R. B. V. Dreele, *J. Appl. Crystallogr.* **2013**, *46*, 544–549.
- [17] B. Ravel, M. Newville, *J. Synchrotron Radiat.* **2005**, *12*, 537–541.

Manuscript received: November 13, 2024

Revised manuscript received: December 17, 2024

Version of record online: January 8, 2025